ARTICLE

Deposition of titanium nitride films using an upscaled magnetized sheet plasma system

Glenson R. Panghulan*[1,2] and Magdaleno R. Vasquez, Jr.[2]

[1]Department of Engineering Science, College of Engineering and Agro-Industrial Technology, University of the Philippines Los Baños, Los Baños, Laguna, 4031 Philippines
[2]Department of Mining, Metallurgical, and Materials Engineering, College of Engineering, University of the Philippines Diliman, Diliman Quezon City, 1101 Philippines

ABSTRACT

Titanium nitride (TiN) is a widely used thin film in different industries. Many studies have examined TiN film growth using conventional deposition systems. However, studies using a magnetized sheet plasma system (MSPS) to grow TiN films with Ti as the sputtering target remain limited. In this work, MSPS sputter deposition parameters such as plasma current (4 and 6 A) and argon:nitrogen (Ar:N_2) flow rate ratios (125:25, 100:50) were correlated with the properties of the resulting TiN films. Raman spectral analyses, x-ray diffraction, scanning electron microscopy, and energy-dispersive spectral analyses revealed that films deposited at 6 A and higher Ar content (125:25) exhibited strong (220) preferred orientation with a crystallite size of 2.13 nm and thickness of 0.94 µm. Films deposited at 4 A and high N_2 content (100:50) showed smaller crystallites (0.28 nm) and thinner films (0.20 µm). The (TA+LA)/TO Raman ratio and EDS results indicated that high N_2 content (100:50) produced nitrogen-rich films (Ti:N ≈ 0.50–0.76), whereas higher argon flow and plasma current yielded near-stoichiometric TiN (Ti:N ≈ 0.81–0.95). These results demonstrate that plasma current and gas-flow ratio strongly govern the structural evolution and stoichiometry of TiN films in the MSPS.

INTRODUCTION

Titanium nitride (TiN) has been of great interest of researchers for several decades. This is because it exhibits high hardness, good chemical stability, good corrosion resistance, good electrical conductivity, and excellent diffusion resistance (Grosso et al. 2017; Chaudry et al. 2018, Kearney et al. 2018). Due to these properties, TiN thin films are used in different manufacturing applications, biomedicine (Jeyachandran et al. 2007), environmental (Panghulan et al. 2021), and microelectronic industries. There are different methods in producing TiN thin films such as chemical vapor deposition (CVD) (Kilicaslan et al. 2019), RF magnetron sputtering (Panghulan et al. 2021), DC magnetron sputtering (Grosso et al. 2017), and high power impulse magnetron sputtering (He et al. 2019). Another method that has not been fully explored for nitride thin-film deposition is the use of a magnetized sheet plasma device (Noguera and Ramos 2006; Ramos and Awayan 2002; Barra and Ramos 2011). The magnetized sheet plasma system (MSPS) is characterized by its ability to generate high-density plasma ($n_e \approx 10^{11} - 10^{13}$ cm^{-3}) while maintaining significant temperature gradients (0.5 to 8 eV) (Abate and Ramos, 2000).

A defining characteristic of the MSPS is the presence of a 'hot electron' population within the sheet core. These are primary electrons originating from the thermionic emission at the tungsten filament cathode, that are subsequently accelerated by the discharge potential. These hot electrons are effectively confined by the magnetic mirror field, allowing them to oscillate within the plasma sheet. This confinement prevents rapid energy loss to the chamber walls and maintains a high-energy population, which is sufficient to drive the high ionization degree of Ar and Ti species. This population facilitates the formation of crystalline TiN on the substrate without requiring external heating (Noguera and Ramos, 2006, Noguera et al. 2008).

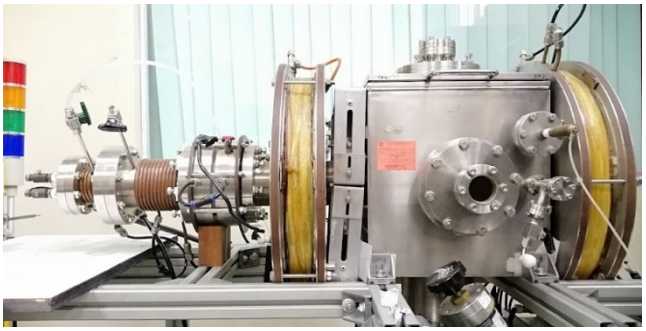

Figure 1: Actual image of the upscaled MSPS.

In this study, an upscaled magnetized sheet plasma system was used to deposit the TiN thin films. Whereas previous studies used a 1L deposition chamber, the upscaled MSPS uses a 10L deposition chamber. The sheet plasma was produced by the resultant magnetic field of a pair of strong dipole magnets and a pair of Helmholtz

Corresponding author
Email Address: **grpanghulan@up.edu.ph**
Date received: 25 January 2026
Date revised: 10 March 2026
Date accepted: 17 March 2026
DOI: https://doi.org/10.54645/2026191NUA-69

KEYWORDS

TiN, Thin films, Sheet Plasma

coils. The sputtering ions were accelerated onto the target by the target bias and the wide-area plasma will enhance the formation of TiN since the hot electrons are confined inside the magnetic field. The confinement of these hot electrons makes the plasma hotter than the conventional plasma methods, making it possible to develop crystalline TiN without substrate heating (Ramos and Awayan 2002). In addition, this study explores the effect of deposition parameters such as Ar:N2 gas ratio and plasma current on the structure and chemical composition of the deposited thin films.

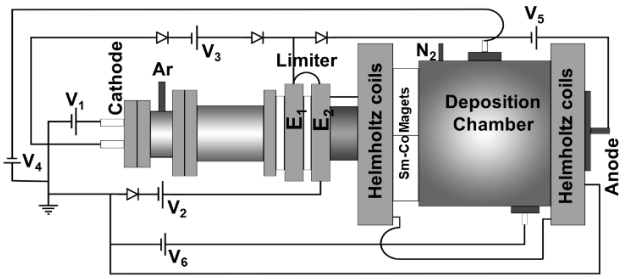

Figure 2: Schematic diagram of the magnetized sheet plasma system used for TiN thin film deposition. V1 is Filament voltage/current source, V2 is the Helmholtz coils, and limiter coil current source, V3 is the limiter electrode bias, and the production chamber, discharge potential, V4 is the target bias, V5 is the anode bias, and V6 is the substrate bias.

MATERIALS AND METHODS

Thin Film Deposition

The TiN thin films were deposited on pre-cleaned glass and silicon (Si) substrates using the MSPS. The MSPS is composed of four main components: the plasma production chamber, plasma limiters, magnet system, and deposition chamber as described in the works of Ramos, Barra and Noguera (Noguera and Ramos 2006; Ramos and Awayan 2002; Barra and Ramos 2011). The system is shown schematically in Fig. 2, while an actual image is presented in Fig. 1.

In the plasma production chamber, a 0.50 mm diameter tungsten (W) filament cathode initiates the discharge via thermionic emission. The plasma limiters (E1 and E2) play a dual role. They house a circular ferrite magnet and a coreless magnetic coil to reinforce the magnetic mirror field, thereby enhancing plasma quiescence and stability. Furthermore, the limiters feature a 1.0 cm aperture that creates a pressure gradient between the production chamber and the deposition chamber.

The magnet system utilizes Helmholtz coils to generate a magnetic mirror field, which works in conjunction with a pair of Sm-Co dipole magnets (1.5 kG surface field). These opposing fields compress the cylindrical plasma into a sheet several millimeters thick over a wide area. Finally, the deposition chamber houses the titanium (Ti) target, the substrate stage, and the anode. The Ti target was biased to facilitate effective sputtering by the high-density argon ions.

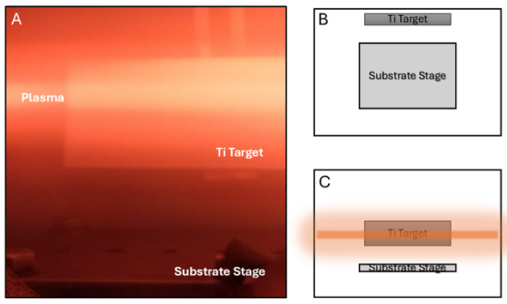

Figure 3: (A) Actual image of the deposition chamber viewed through the viewport; (B) top-view schematic of the target and substrate configuration; and (C) front-view schematic.

The substrate was positioned off-axis, approximately 3 cm below the Ti target and parallel to the sheet plasma core. This configuration (shown in the schematic top and front views in Fig. 3) was chosen to prevent direct exposure to the high-energy primary electrons at the sheet core while remaining within the region of the plasma.

Glass and rough Si substrates were cut to 1 x 1 cm^2 sizes and ultrasonically cleaned in a series of acetone, ethanol, and water baths for 15 min each. A high purity Ti (99.6%, Advent Research Materials Ltd) target was used as Ti source. Mixtures of 99.99% argon (Ar) and 99.99% nitrogen (N_2) were introduced to the MSPS after the system reached a base pressure below 3 x 10^{-3} Pa. The remaining deposition parameters used during deposition are listed in Table 1. The deposition time was set at 180 min.

Table 1: Deposition parameters used for TiN film growth

Parameter	Settings
Target	99.6% Ti
Ar:N_2 gas flow rate (sccm)	125:25, 100:50
Plasma current V5 (A)	4, 6
Target bias, V4 (kV)	-1
Substrate bias, V6 (V)	-150
Working pressure (Pa)	1
Base pressure (Pa)	<3 x 10^{-3}
Deposition time (min)	180

Characterization

Optical emission spectrometer (OES) was used to analyze the generated sheet plasma. One end of the fiber optic cable of the Ocean Optics USB4000 was positioned on a viewport of the MSPS such that its line of sight was parallel to the sheet plasma. The other end of the fiber was connected to the spectrometer. The emission spectrum was recorded from 350 to 1050 nm.

Field-emission scanning electron microscopy (FE-SEM, Hitachi SU8230) was used to observe the microstructure and measure film thickness. Elemental mapping was performed using the energy dispersive spectroscopy (EDS, Horiba XMax N) attached to the SEM device. The film structure was analyzed by Raman spectroscopy (Horiba LabRAM HR Evolution). The Raman measurement was performed using a 532 nm laser at 10% power with an acquisition time of 30 sec over a spectral range of 100-1000 cm^{-1}. X-ray diffraction (XRD) measurement (PANalytical's X'Pert PRO) was carried out using Cu Kα (1.5406 ˚A) radiation, and 2θ was scanned from 35◦ to 65◦ with a step size of 0.02˚. The nanoindentation hardness of the thin film was investigated using a nanoindenter (TI-900, TriboIndenter, Hysitron) with a Berkovich 142.3° diamond probe.

RESULTS

Optical Emission Spectroscopy

TiN films were deposited using the MSPS, and the resulting plasma was analyzed by OES. Fig. 4(a) shows the optical emission spectra of the gas discharge during the deposition. The spectral lines at 696, 706, 795, 801, 811, 827, 841, and 883 nm correspond to the first ionization of Ar (Ar I), the transition from 2p–1s (Hubilla et al. 2018, Osonio and Vasquez 2018). The broad bands at 550 to 780 nm correspond to the first positive system ($B^3\pi_g \rightarrow A^3\Sigma^+_u$) of N (Dhasiyan et al. 2024). The peak at 520 nm is the emission wavelength of Ti ions (Ren How et al. 2018) indicating sputtering and post-ionization of the Ti target.

Fig. 4(b) shows the comparison of the intensities of selected peaks for Ar, N_2, and Ti. A higher plasma current increased ion intensities and, consequently, the current density (Hanai et al. 2020). As current density increases, the ion velocity also increases (Goebel and Katz 2008). This increased the probability of ionization,

leading to a higher sputtering yield. High Ar content in the system increased the Ti intensity owing to the higher sputtering yield of Ar (Ramos and Ayawan 2002). Figs. 4.c and 4.d show the line intensity ratios of different transitions. It can be used to measure relative variation among the active species in the gas discharge. No significant difference was observed when changing the plasma current for the Ar:N_2 line ratio. However, increased Ti:Ar and Ti:N_2 ratios were observed with increasing plasma current and argon content.

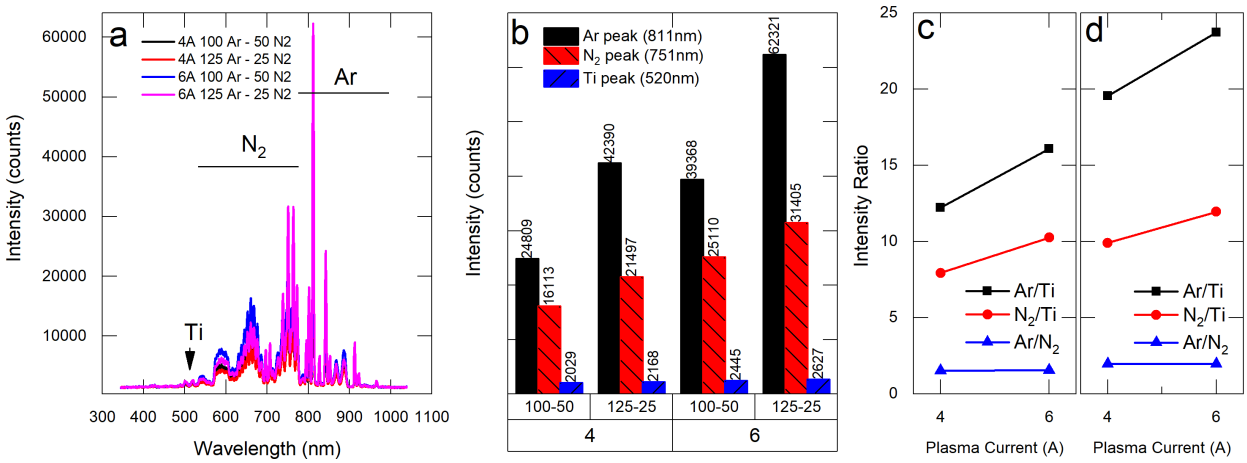

Figure 4: Optical emission spectra (a), intensities of Ti, Ar, and N_2 lines (b), and line-intensity ratios of selected Ti, N_2, and Ar spectral lines at (c) 100 Ar:50 N_2 and (d) 125 Ar:25 N_2 under different plasma currents.

Raman Spectroscopy

In a pure, stoichiometric TiN, no Raman signal can be detected due to its crystal structure. The FCC structure has an inverted site symmetry; as such, the polarizability does not change with vibrational mode. However, vacancies break the structural symmetry, allowing TiN Raman modes to appear (Barbosa et al. 2021; Kearney et al. 2018). Since MSPS is a plasma-based deposition technique, the deposited TiN films are expected to be defect-rich. These defects induce the first-order phonons (Vasconcellos et al. 2007)

The Raman spectra shown in Fig. 5 indicate that the synthesized film was consisted solely of TiN thin films. The peaks at 210, 302, and 568 cm^{-1} correspond to the first order phonons: transverse acoustic (TA), longitudinal acoustic (LA), and transverse optical (TO). In several studies (Barbosa et al. 2021; Kearney et al. 2018; Vasconcellos et al. 2007), the Raman peaks at acoustic range (150-300 cm^{-1}) are attributed to Ti ion vibrations in the N-vacancy region, and the optical range (400-650 cm^{-1}) are attributed to the N ion vibrations in the Ti-vacancy region. Estimation of the film Ti:N stoichiometry can be done by calculating the ratio of the area under the acoustic and optical range fitted with a Gaussian-Lorentzian curve as discussed in several studies (Barbosa et al. 2021; Vasconcellos et al. 2007; Cheng et al. 2002). The (TA+LA)/TO ratio suggests that the deposited films are nitrogen-rich.

Furthermore, the peak positions and separations change with deposition parameters. The shift in the TA peak position is due to the titanium vacancies, which causes strain in the lattice.

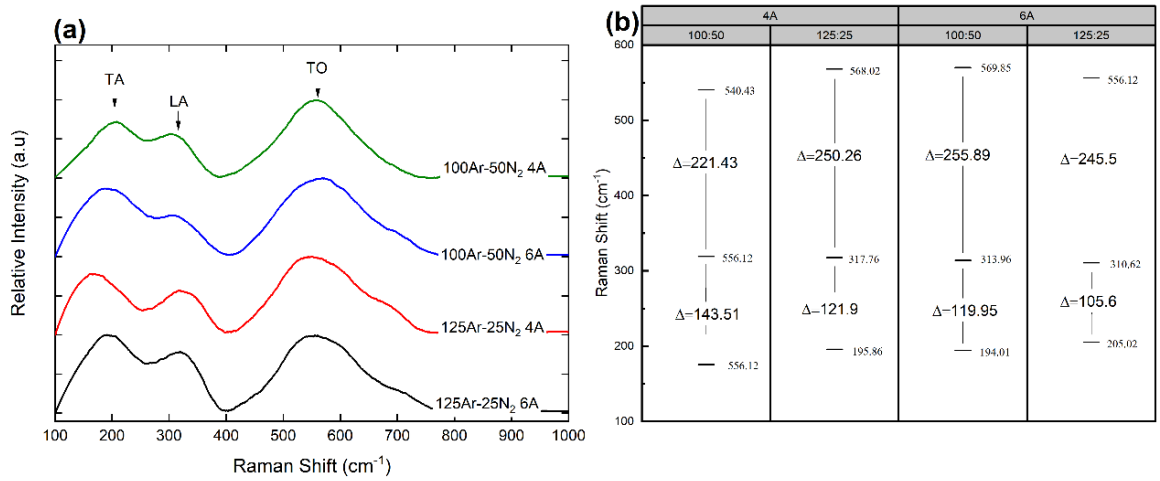

Figure 5: Raman spectra of TiN films

X-ray Diffraction

The crystal structure of the deposited TiN thin films was examined by XRD. Fig. 6(a) shows the XRD patterns of deposited thin films. Peaks at 36.2°, 42.2° and 61.6° are associated with (111), (200), and (220) planes of the TiN cubic phase (Escalona et al. 2021). It is observed in Fig. 6(a) that deposition conditions influence the TiN thin film orientation. At low plasma current, the (111), (200), and (220) TiN peaks are present. However, at a higher plasma current, the films showed a preferred (220) orientation. The crystallite size of TiN was estimated using the Scherrer equation.

$$D = \frac{0.94\,\lambda}{\beta cos\theta}$$

where D is the crystallite size, λ is the X-ray wavelength (0.154056 nm), β is the full width half maximum (FWHM) of diffraction peak in radians, θ is the Bragg's angle. Microstrain was calculated using the following equation (Jeganath and Raviprakash 2021):

$$\epsilon = \frac{\beta cos\,\theta}{4}$$

the microstrain decreases as plasma current and Ar content increase.

Fig. 6(b) shows the crystallite size and microstrain calculated from the (220) plane. It is observed that the crystallite size increases and

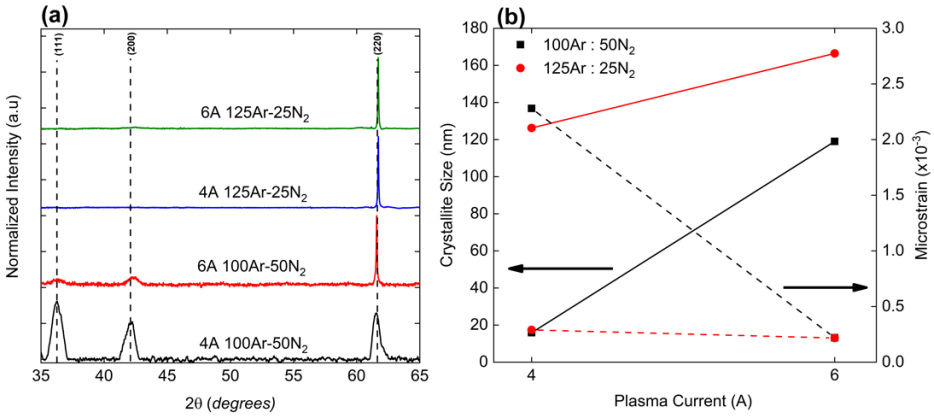

Figure 6: XRD patterns (a) and calculated crystallite size (b) of the deposited thin films

Scanning Electron Microscopy – Energy Dispersive Spectroscopy

Fig. 7 presents the SEM images of the surface morphology and cross-section of the film deposited on rough silicon substrates. Small, globular aggregates were observed. High Ar content (125:25) formed smoother, thicker, and more uniform films. Increasing the plasma current led to thicker and rougher film due to more rapid TiN growth. Increasing N_2 gas content favors the formation of bigger globules.

In the SEM-EDS images of the film shown in the third row of Fig. 7, Ti, N, and substrate Si were detected. The TiN film also appeared uniform across the surface. The Ti:N atomic ratio is shown in Table 2. Low N_2 content and higher plasma current lead to the formation of near stoichiometric TiN. Higher N_2 content and lower plasma current resulted in non-stoichiometric TiN.

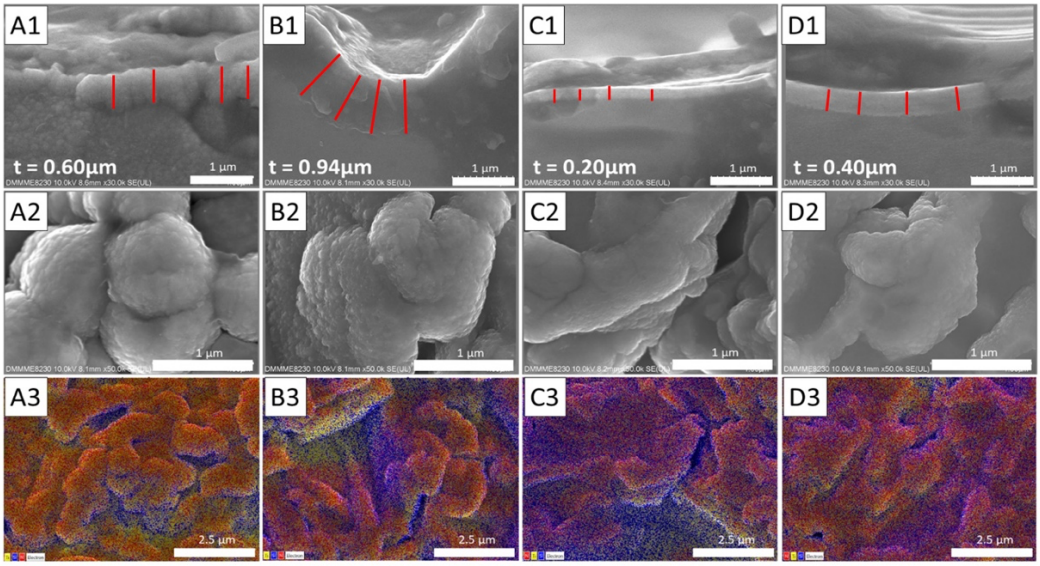

Figure 7: SEM images of the thin films. Row 1 shows cross-sectional views, row 2 shows plan views, and row 3 shows elemental maps. Columns correspond to deposition settings: (A) 100:50–6A, (B) 125:25–6A, (C) 100:50–4A, and (D) 125:25–4A.

Nanoindentation

The mechanical performance of the TiN films deposited at the 6 A current and 125:25 Ar:N_2 ratio was evaluated via nanoindentation. Fig. 8 shows the characteristic load-displacement curve obtained for this sample. Using the Oliver-Pharr method, the hardness was estimated to be approximately 22 GPa. This measured value is comparable to the reported hardness values of TiN which ranges from 20 to 25 GPa. (Dang et al. 2022; Cheng et al. 2010)

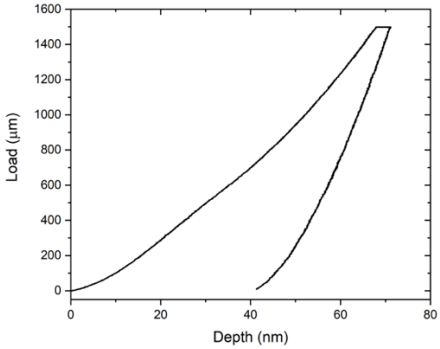

Figure 8: Load-Displacement curve obtained during nanoindentation of sample 125:25-6A

DISCUSSION

Correlation of Results

Table 2 summarizes the OES line ratio, SEM-EDS and Raman Ti/N ratios, film thickness, and XRD crystallite sizes measurement. In general, increasing the energy of the plasma increases the probability of sputtering more target atoms since the current density increases as the plasma current increases, resulting in faster sputtering ions.

Based on the SEM micrograph observations, agglomeration occured on the higher plasma current samples. This agglomeration is due to the high energetic ion flux reaching the substrate surface, thereby promoting crystallite reorganization (Fani and Savaloni 2012). The thickness of the film is correlated to the number of sputtered Ti atoms. The lower thickness observed in lower Ar content is attributed to the reduced number of Ar ions (Diletto et al. 2024), which are the primary sputtering species (Sato et al. 2024).

The Ti:N atomic stoichiometry of the TiN film correlates with the Ti:N_2 line ratio of emission spectra. Since these are the plasma species involved in TiN formation, the amount of excited nitrogen in the spectra is proportional to the amount of nitrogen in the thin film as shown in Fig. 9.

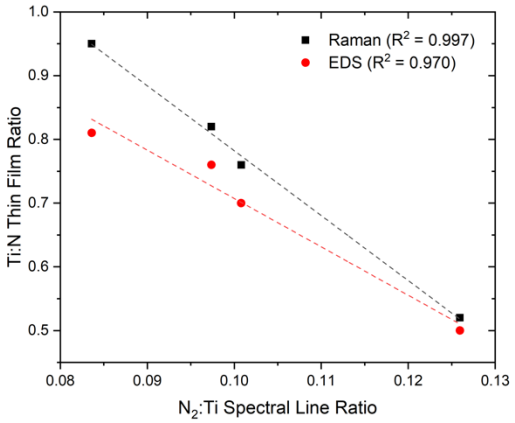

Figure 9: Correlation between the Ti:N_2 optical spectral line ratio and the Ti:N atomic ratio of the deposited thin films measured using Raman and EDS. The dashed lines represent linear fits.

The differences in the Ti:N ratio suggested by Raman spectroscopy and EDS are attributed to the differing sampling depths and physical principles of the two techniques. EDS provides a bulk elemental average over a depth of less than about 3 µm. Conversely, Raman spectroscopy of TiN is highly sensitive to the near-surface region and lattice symmetry (Babichuk et al. 2020). In TiN, Raman activity is primarily induced by nitrogen ions vibrating in the vicinity of titanium vacancies. The high (TA+LA)/TO ratios observed indicate an N-rich surface environment. Therefore, the films are characterized by a stoichiometric bulk with a nitrogen-rich surface termination, a common occurrence in plasma-enhanced deposition due to late-stage nitrogen immersion (Belahcen et al. 2020).

The increase in crystallite size of a deposited thin film is influenced by three major parameters: substrate temperature, ion bombardment rate, and energy flux (Ajenifuja et al. 2019). While the experiment setup did not utilize an external substrate heater, the substrate was being heated by the bombardment of energetic ions and the recombination of reactive species (Shapovalov and Sharkovskii 2024; Cui et al. 2023).

This energy flux is directly proportional to the plasma current; as the current was increased from 4 A to 6 A, the ion flux density intensified, leading to a higher effective substrate temperature (Manova et al, 2010, Brown et al, 2021). This elevated local temperature enhances adatom mobility on the growing film surface, facilitating the transition from low-crystallinity films to more crystalline films observed at 6 A (Lee et al. 2026; Cui et al. 2023). Similarly, at high Ar content, intensive argon ion bombardment increases the crystallite size. Thus, the plasma current and argon ion bombardment act as sources of thermal energy for the structural evolution of TiN thin films.

This increase in energy also accounts for the observed reduction in microstrain at higher plasma current and Ar concentration. Microstrain typically originates from lattice distortions caused by defects, such as vacancies or atoms trapped in non-equilibrium interstitial positions during rapid deposition (Lee et al., 2025). The intensified ion bombardment and intrinsic plasma driven heating acts as an in-situ annealing mechanism. This provides the necessary activation energy for atoms to migrate from these metastable, strained positions into their equilibrium lattice sites.

As the atoms arrange themselves, the local variations in lattice spacing decrease, leading to the measured reduction in microstrain. Therefore, the higher energy at 6 A not only promotes the growth of larger crystallites but also facilitates structural relaxation, resulting in a higher quality, less distorted crystal lattice (Lee et al. 2025; Lee et al. 2026; Cui et al. 2023).

The preferred crystallographic orientation of the film is governed by the minimizaation of overall surface, strain, and stopping energies of the lattice planes. In the TiN lattice, the lowest surface, strain, and stopping energies are from the (200), (111), and (220) planes, respectively (Khojier et al.2013). Since the increase in plasma current and argon content leads to an increase in energy in the plasma, thus, the deposited ions have higher energy. This higher energy makes stopping energy dominant and orient the films to the (220) plane.

Table 2: Measured quantities from the spectroscopic, microscopic, and XRD analysis of the deposited TiN thin films

Deposition Conditions		Thin Film Ti:N Ratio		Ratio of Plasma Species			Thickness (µm)	Crystallite size (nm)
Ar:N2 gas flow (sccm)	Plasma current (A)	Raman	EDS	Ar:N2	Ti:Ar	Ti:N_2		
125:25	4	0.76	0.70	1.97	19.55	0.101	0.40	1.84
125:25	6	0.95	0.81	1.98	23.72	0.084	0.94	2.13
100:50	4	0.52	0.50	1.54	12.23	0.126	0.20	0.28
100:50	6	0.82	0.76	1.57	16.10	0.097	0.60	2.10

Comparison with the Lab-Scale Prototype MSPS

Data for TiN deposition using the lab-scale prototype are presented. One of the major challenges of upscaling plasma systems is maintaining a stable plasma. From the process parameter of the lab-scale prototype, at a plasma current of 2.5 A and a working pressure of 5.33 Pa, it was not possible to have a stable plasma in the upscaled system using the parameters employed in the lab-scale prototype. Upscaling plasma systems leads to changes in the electrical parameters of the discharge.

Table 3: Comparison of process parameter and results of the lab-scale prototyped MSPS and the upscaled MSPS.

System	Plasma Current (A)	Working Pressure (Pa)	Deposition Rate (μm/min)	Prominent XRD Peaks
Lab-scale	2.5 – 4	5.33	0.345	(200) (220) (311)
Lab-scale	4	4.66	0.166	(200) (220) (311)
Lab-scale	2 – 3	5.333	N/A	(200)
Upscale	4 – 6	1.00	0.005	(220)

The instability of the plasma at the upscaled prototype using the lab-scale prototype process parameters may be associated with the different residence time. Residence time is the average time for which a molecule of a flowing gas remains in a chamber before being pumped out of the chamber (Knoops et al. 2015). It can be estimated using the equation below (Corbella 2014):

$$t = \frac{V}{S}$$

Where t is the residence time, V is the volume of the chamber, and S is the pumping speed. The main differences between the upscaled and lab-scale prototypes are the chamber sizes and vacuum pump used. The lab-scale prototype has a deposition chamber of 1L and an estimated pumping speed of 125 L/s, while the upscaled prototype has a deposition chamber of 10L and an estimated pumping speed of 685 L/s. The residence times for the lab-scale prototype and upscaled prototype are 0.008 s and 0.015 s, respectively. This means that the gas molecules evacuate faster in the lab-scale prototype.

Although the difference in residence time is numerically small (~7 ms), it is significant within the context of plasma kinetics. In MSPS, where ionization and molecular dissociation occur on microsecond timescales, an additional 7 ms of residence time fundamentally alters the probability of secondary collisions and reactive species formation. Residence time should ideally be controlled because it plays an important role in plasma kinetics and reactions.

The difference between the estimated residence time may appear small, yet it can still produce a large disparity in deposition rate. However, there is a variation between the working pressure. Working pressure influences the deposition rate. Higher working pressure can increase the deposition rate because of the greater number of gas molecules and more frequent collisions between gas molecules and the target surface. The combination of high working pressure and low gas residence time led to stable plasma at low current settings and a faster deposition rate, as observed in the lab-scale prototyped MSPS machine.

The reduction of deposition rate from 0.345 μm/min to 0.005 μm/min can also be attributed to the geometric dilution and the reduced ion-flux density in the upscaled prototype. In the 1L lab-scale prototype, the plasma is highly confined, resulting in a high density of ions per unit area. In the 10L upscaled prototype, the plasma volume expands, distributing the plasma current over a larger spatial region. Consequently, the number of Ar+ ions bombarding the titanium target per second decreases, thereby lowering the sputtering rate. Furthermore, the sputtered titanium atoms must travel through a larger space where they are subject to geometric dilution. In geometric dilution, a greater proportion of the material is lost to the expanded chamber walls rather than being intercepted by the substrate (Bouazza 2023). This reduction in arriving flux, combined with the lower working pressure (1 Pa), drives the observed decrease in growth rate.

Industrial throughput can be significantly enhanced by operating at higher deposition rate regimes. Specifically, increasing the plasma current beyond 6 A would increase the ion flux density, thereby accelerating the sputtering yield. Furthermore, scaling the target geometry and optimizing the target-to-substrate distance would minimize geometric dilution. While higher rates and prolonged bombardment can influence intrinsic stress, the MSPS's ability to promote preferred crystallographic orientations (220) suggests that high-quality, dense films can still be achieved at reduced deposition times through further power and geometric optimization.

The accumulation of intrinsic stress, a common challenge in plasma deposition processes, can be mitigated in this system. The intrinsic plasma-driven heating observed in the MSPS serves as an in-situ annealing mechanism, promoting continuous lattice relaxation and reducing microstrain during the growth process (Khalil and Wanas, 2025; Lee et al., 2025; Lee et al., 2026; Cui et al., 2023). For future industrial applications requiring even thicker coatings, stress can be further managed by incorporating a thin metallic Ti buffer layer to bridge the thermal expansion mismatch between the TiN film and the substrate.

CONCLUSION

TiN thin films were successfully deposited using the upscaled magnetized sheet plasma system. Variation of deposition parameters produced films with distinct structural and compositional characteristics. At low plasma current (4 A) and high N_2 content (100:50), the films exhibited low crystallinity with small crystallite size (~0.28 nm), thin films (~0.20 μm), and nitrogen-rich composition (Ti:N ≈ 0.50–0.52). In contrast, increasing the plasma current to 6 A and the Ar content to 125:25 produced highly textured (220) films with larger crystallite size (~2.13 nm), thicker films (~0.94 μm), and near-stoichiometric composition (Ti:N ≈ 0.95).

Higher plasma current increased ion flux and sputtering yield, leading to faster deposition and rougher but more crystalline films. The combined Raman, EDS, and OES analyses consistently showed that low N_2 content and high current conditions favored stoichiometric TiN formation, while high N_2 content and low current conditions promote N-rich films.

Overall, the upscaled MSPS enables tunable TiN film properties through simple control of plasma current and Ar:N_2 ratio, providing a viable route for optimizing TiN coatings for specific industrial applications.

ACKNOWLEDGMENTS

The authors acknowledge the support of the Department of Science and Technology (DOST) Philippine Council for Industry, Energy and Emerging Technology Research and Development (PCIEERD) CRADLE PROJECT: Enhancement and Market Validation of Plasma Enhanced Chemical Vapor Deposition Industrial Prototype for Nitride-based Coatings. We also acknowledge the CHED PCARI Nanoquench Project for the Raman Spectroscopy. G. Panghulan acknowledges the DOST - Science Education Insitute (SEI) - Engineering Research and Development for Technology (ERDT). M. Vasquez acknowledges the Dado and Maria Banatao Professorial Chair in Engineering

CONFLICT OF INTEREST

The authors declare that they have no known competing financial interests or personal relationships that could have appeared to influence the work reported in this paper.

CONTRIBUTIONS OF INDIVIDUAL AUTHORS

Glenson R. Panghulan: Conceptualization, Data curation, Formal Analysis, Investigation, Methodology, Software, Visualization, Writing – original draft.
Magdaleno R. Vasquez Jr.: Conceptualization, Funding acquisition, Project administration, Resources, Supervision, Validation, Writing – review & editing.

REFERENCES

Abate Y, Ramos H. Optimization and enhancement of H − ions in a magnetized sheet plasma. Rev Sci Instrum 2000; 71(10). https://doi.org/10.1063/1.1289510.

Ajenifuja E, Popoola API, Popoola OM. Thickness dependent chemical and microstructural properties of DC reactive magnetron sputtered titanium nitride thin films on low carbon steel cross-section. J Mater Res Technol 2019; 8(1):377-384. https://doi.org/10.1016/j.jmrt.2018.02.010.

Babichuk IS, Semenenko MO, Caballero R, Datsenko OI, Golovynskyi S, Qiu R, Huang C, Hu R, Babichuk IV, Ziniuk RR, Stetsenko M, Kapush OA, Yang J, Li B, Qu J, Leon M. Raman mapping of MoS2 at Cu2ZnSnS4/Mo interface in thin film. Sol Energy 2020; 205:154-160. https://doi.org/10.1016/j.solener.2020.05.043.

Barbosa MGC, Viana BC, Santos FEP, Fernandes F, Feitor MC, Costa THC, Sousa RRM. Surface modification of tool steel by cathodic cage TiN deposition. Surf Eng 2021; 37(3):334-342. https://doi.org/10.1080/02670844.2019.1663011.

Barra HMD, Ramos HJ. Deposition rate and energy enhancements of TiN thin-film in a magnetized sheet plasma source. Int J Mater Metall Eng 2011.

Belahcen S, Vallée C, Bsiesy A, Chaker A, Jaffal M, Yeghoyan T, Bonvalot M. Control of ion energy during plasma enhanced atomic layer deposition: a new strategy for the modulation of TiN growth delay on SiO2. J Vac Sci Technol A 2021; 39(1): 012410. https://doi.org/10.1116/6.0000655.

Brown R, Lönn B, Pfeiffer R, Frederiksen H, Wickman B. Plasma-induced heating effects on platinum nanoparticle size during sputter deposition synthesis in polymer and ionic liquid substrates. Langmuir 2021; 37(29):8821-8828. https://doi.org/10.1021/acs.langmuir.1c01190.

Bouazza A. Revealing the role of vacuum chamber parameters on the pathways leading to substrate deposition by ejected atoms. Int J Thin Film Sci Technol 2023; 12(3):159-162. https://doi.org/10.18576/ijtfst/120301.

Chaudhry AU, Mansoor B, Mungole T, Ayoub G, Field DP. Corrosion mechanism in PVD deposited nano-scale titanium nitride thin film with intercalated titanium for protecting the surface of silicon. Electrochim Acta 2018; 264:69-82. https://doi.org/10.1016/j.electacta.2018.01.042

Cheng YH, Tay BK, Lau SP, Kupfer H, Richter F. Substrate bias dependence of Raman spectra for TiN films deposited by filtered cathodic vacuum arc. J Appl Phys 2002; 92(4):1845-1849. https://doi.org/10.1063/1.1491588.

Cheng Y, Chen JW, Tay BK. Mechanical and tribological properties of TiN/Ti multilayer coating deposited by filtered cathodic vacuum arc. Surf Coat Technol 2010; 204(12-13):1962-1969. https://doi.org/10.1016/j.surfcoat.2009.11.015.

Corbella C. Upscaling plasma deposition: the influence of technological parameters. Surf Coat Technol 2014; 242:237-245. https://doi.org/10.1016/j.surfcoat.2013.12.002.

Cho S, Park HK, An S, Hong SJ. Plasma ion bombardment induced heat flux on the wafer surface in inductively coupled plasma reactive ion etch. Appl Sci 2023; 13(17):9533. https://doi.org/10.3390/app13179533.

Dang NM, Lin WY, Wang ZY, Alidokht SA, Chromik RR, Chen TYF, Lin MT. Mechanical properties and residual stress measurement of TiN/Ti duplex coating using HiPIMS TiN on cold spray Ti. Coatings 2022; 12(6):759. https://doi.org/10.3390/coatings12060759.

Dhasiyan AK, Amalraj FW, Jayaprasad S, et al. Epitaxial growth of high-quality GaN with a high growth rate at low temperatures by radical-enhanced metalorganic chemical vapor deposition. Sci Rep 2024; 14:10861. https://doi.org/10.1038/s41598-024-61501-9.

Diletto C, Nunziata F, Aprano S, Migliaccio L, Maglione MG, Rubino A, Tassini P. Influence of process parameters on properties of non-reactive RF magnetron-sputtered indium tin oxide thin films used as electrodes for organic light-emitting diodes. Crystals 2024; 14(9):776. https://doi.org/10.3390/cryst14090776.

Escalona M, Bhuyan H, Ibacache S, Retamal MJ, Saikia P, Borgohain C, Valenzuela JC, Veloso F, Favre M, Wyndham E. Study of titanium nitride film growth by plasma enhanced pulsed laser deposition at different experimental conditions. Surf Coat Technol 2021; 405:126492. https://doi.org/10.1016/j.surfcoat.2020.126492.

Fani N, Savaloni H. Investigation on the formation of titanium nitride thin films on 304 type stainless steel using plasma focus device. J Theor Appl Phys 2012; 6:30. https://doi.org/10.1186/2251-7235-6-30.

Khalil S, Wanas A. Influence of magnetron DC sputtering conditions and annealing on the structural, morphological, and optical properties of Ag/Au thin films. Perinat J 2025; 33(2):594-602 https://doi.org/10.57239/prn.25.03320065.

Goebel DM, Katz I. Fundamentals of electric propulsion: ion and Hall thrusters. JPL Space Sci Technol Ser 2008.

Grosso S, Latu-Romain L, Berthomé G, Renou G, Le Coz T, Mantel M. Titanium and titanium nitride thin films grown by dc reactive magnetron sputtering physical vapor deposition in a continuous mode on stainless steel wires: chemical, morphological and structural investigations. Surf Coat Technol 2017; 324(15):318-327. https://doi.org/10.1016/j.surfcoat.2017.05.089.

Hanai K, Ishihara S, Endo R, Takimoto T, Tonegawa A, Sato K. Development of Cs-free negative-ion source by sheet plasma. Plasma Fusion Res 2020; 15:2401029. https://doi.org/10.1585/pfr.15.2401029.

He Z, Zhang S, Sun D. Effect of bias on structure mechanical properties and corrosion resistance of TiNx films prepared by ion source assisted magnetron sputtering. Thin Solid Films 2019; 676:60-67. https://doi.org/10.1016/j.tsf.2019.02.037.

Hubilla FAD, Panghulan GR, Pechardo J, Vasquez MR. Mechanical properties of epoxy composites with plasma-modified rice-husk-derived nanosilica. Jpn J Appl Phys 2018; 57(1S):01TB05. https://doi.org/10.7567/JJAP.57.01AG07.

Jeganath K, Raviprakash Y. Near-optimal composition of CZTS thin film via exploration of copper and thiourea molar concentration in spray pyrolysis technique. Mater Res Express 2021; 8(11):116404. https://doi.org/10.1088/2053-1591/ac343e.

Jeyachandran YL, Venkatachalam S, Karunagaran B, Narayandass SK, Mangalaraj D, Bao CY, Zhang CL. Bacterial adhesion studies on titanium, titanium nitride and modified hydroxyapatite thin films. Mater Sci Eng C 2007; 27(1):35-41. https://doi.org/10.1016/j.msec.2006.01.004.

Kearney BT, Jugdersuren B, Culbertson JC, Desario PA, Liu X. Substrate and annealing temperature dependent electrical resistivity of sputtered titanium nitride thin films. Thin Solid Films 2018; 661:78-83. https://doi.org/10.1016/j.tsf.2018.07.001.

Khojier K, Savaloni H, Shokrai E, et al. Influence of argon gas flow on mechanical and electrical properties of sputtered titanium nitride thin films. J Theor Appl Phys 2013; 7:37. https://doi.org/10.1186/2251-7235-7-37.

Kilicaslan A, Zabeida O, Bousser E, Schmitt T, Klemberg-Sapieha JE, Martinu L. Hard titanium nitride coating deposition inside narrow tubes using pulsed DC PECVD processes. Surf Coat Technol 2019; 377:124894. https://doi.org/10.1016/j.surfcoat.2019.124894.

Knoops HCM, de Peuter K, Kessels WMM. Redeposition in plasma-assisted atomic layer deposition: silicon nitride film quality ruled by the gas residence time. Appl Phys Lett 2015; 107:014102. https://doi.org/10.1063/1.4926366.

Lee DK, Fykouras K, Kodalle T, Moral RF, Schwartz CP, Tamura N, Lawler KV, Leppert L, Sutter-Fella CM. Reduction of microstrain at the perovskite surface via alkali metal chloride treatment enhances stability. ACS Energy Lett 2025; 10(3):1039-1049. https://doi.org/10.1021/acsenergylett.4c03334.

Lee G, Yoo J, Choi H, Kim J, Cho M. In-situ post-doping plasma process during atomic layer deposition of Al-doped TiO2 for sub-nanometer lattice ordering and defect annihilation. Int J Extrem Manuf 2026; 8(1):015101. https://doi.org/10.1088/2631-7990/ae037b.

Manova D, Gerlach JW, Mändl S. Thin film deposition using energetic ions. Materials 2010; 3(8):4109-4141. https://doi.org/10.3390/ma3084109.

Noguera VR, Ramos HJ. A magnetized sheet plasma source for the synthesis of TiN on stainless steel substrates. Thin Solid Films 2006; 506-507:613-616. https://doi.org/10.1016/j.tsf.2005.08.048.

Noguera VR, Blantocas G, Ramos H. Optimized H- extraction in an argon-magnesium seeded magnetized sheet plasma. Nucl Instrum Methods Phys Res A 2008; 266:2627-2637. https://doi.org/10.1016/j.nimb.2008.01.037

Osonio AP, Vasquez MR. Effects of discharge-forming gases on the antibacterial sensitivity of plasma-reduced silver impregnated in natural zeolites. J Mater Sci 2018; 53:11280-11291. https://doi.org/10.1007/s10853-018-2419-9.

Panghulan GR, Vasquez MR, Edañol YD, Chanlek N, Payawan LMS. Synthesis of TiN/N-doped TiO2 composite films as visible light active photocatalyst. J Vac Sci Technol B 2020; 38(6):062203. https://doi.org/10.1116/6.0000304.

Ramos HJ, Awayan R. Nitride formation using a magnetized sheet plasma source. Vacuum 2002; 65(3-4):397-402. https://doi.org/10.1016/S0042-207X(01)00448-1.

Ren How S, Nayan N, Lias J, Khairul Ahmad M, Zainizan Sahdan M, Hafiz Mamat M, Rusop Mahmood M, Aldalbahi A. Plasma diagnostic by optical emission spectroscopy on reactive magnetron sputtering plasma – a brief introduction. J Phys Conf Ser 2018; 1027:012005. https://doi.org/10.1088/1742-6596/1027/1/012005.

Sato T, Igarashi S, Takahashi K, Mukaigawa S, Takaki K. Production of high-power nitrogen sputtering plasma for TiN film preparation. Processes 2024; 12(7):1314. https://doi.org/10.3390/pr12071314.

Shapovalov VI, Sharkovskii DS. Study of heat flow at substrate during sputtering of copper–titanium sandwich target. Materials 2024; 17(14):3599. https://doi.org/10.3390/ma17143599.

Vasconcellos MA, Hinrichs R, Javorsky CS, Giuriatti G, Borges da Costa JA. Micro-Raman characterization of plasma nitrided Ti6Al4V-ELI. Surf Coat Technol 2007; 202(1):275-279. https://doi.org/10.1016/j.surfcoat.2007.05.038.